Check for updates

The importance of electrolyte environment during *in situ* self-transformation for synthesizing V$_2$O$_5 \cdot n$H$_2$O†

Haijia Quan, [ID] Chen Wang, [ID] Dongxu Guo, Xiaofeng Wang, [ID] Chenglin Sun* and Shenghan Wang [ID] *

V$_2$O$_5 \cdot n$H$_2$O is a promising cathode material for zinc-ion batteries. One of the synthesis methods of V$_2$O$_5 \cdot n$H$_2$O is *in situ* self-transformation. In this communication, we focus on the influence of the electrolyte environment during *in situ* self-transformation (from VO$_2$ to V$_2$O$_5 \cdot n$H$_2$O). 2 M ZnSO$_4$ and 2 M Zn(OTf)$_2$ were used as different electrolytes to produce VOH-1 and VOH-2. VOH-1 expands in volume along the electric field to form a porous surface structure and shows low crystallinity along the (0 0 1) plane, while VOH-2 exhibits the opposite. These advantages enable the assembled batteries with VOH-1 to maintain excellent cycling performance at a rate of 2 A g^{-1} with a capacity of 500 mA h g^{-1} and stable cycling for 1800 cycles.

Zinc-ion batteries have garnered considerable attention because of their environmental friendliness, safety and cost effectiveness. However, several significant challenges must be addressed before practical applications can be realized. Among these challenges, the development of cathode materials, a crucial component in zinc-ion batteries, takes precedence. Notably, V$_2$O$_5 \cdot n$H$_2$O emerges as one of the most promising candidates, attracting wide interest.[1–5] As a representative layered material, V$_2$O$_5 \cdot n$H$_2$O exhibits an excellent interlayer structure (between the (0 0 1) planes) to accommodate Zn^{2+}.[6–10] The H$_2$O between the (0 0 1) planes stabilizes the primary structure of V$_2$O$_5 \cdot n$H$_2$O and significantly reduces electrostatic repulsive force through a "charge shield effect".[7,8]

Unlike conventional synthesis methods, *in situ* self-transformation oxidizes V^{4+} to V^{5+} electrochemically. In certain cases, structural H$_2$O can be incorporated into newly formed materials.[11,12] However, researchers have focused mainly on the control of precursors, while the regulation of the electrolyte

environment during *in situ* self-transformation has been largely overlooked.[13,14] It is much simpler to adjust the electrolyte environment than to create a better precursor. Producing V$_2$O$_5 \cdot n$H$_2$O through adjusting the electrolyte environment eliminates complicated synthesis steps.

This work used 2 M ZnSO$_4$ and 2 M Zn(OTf)$_2$ as electrolytes during *in situ* self-transformation, resulting in distinct V$_2$O$_5 \cdot n$H$_2$O. The importance of the electrolyte environment during *in situ* self-transformation for synthesizing V$_2$O$_5 \cdot n$H$_2$O is demonstrated by contrasting the differences between VOH-1 and VOH-2. Through the analysis of the morphology and structure, we discover that VOH-1 has a porous surface structure, expanded volume and lower crystallinity along the (0 0 1) plane. VOH-1 exhibits a tendency to grow along the electric field. On the contrary, VOH-2 shows a reduction in volume and higher crystallinity along the (0 0 1) plane. The electrochemical characterization further illustrates the importance of the electrolyte environment during *in situ* self-transformation.

The precursor of *in situ* self-transformation was synthesized following a previously established protocol.[15] The SEM images of the VO$_2$ powder and VO$_2$ electrode revealed that VO$_2$ is well dispersed in super P (Fig. S1a$_1$, a$_2$, b$_1$ and b$_2$, ESI†). Dark clusters are identified as super P. The XRD pattern of the VO$_2$ powder is well indexed to VO$_2$ (PDF#04-007-2429) (Fig. S2a$_1$, ESI†). After the VO$_2$ electrode was prepared, the XRD peaks of the (1 1 0), (2 2 0) and (3 3 0) planes exhibit higher intensity, resulting from crystal orientation caused by the electrode preparation process (Fig. S2a$_2$, ESI†). The Raman spectra of VO$_2$ are consistent with previous reports (Fig. S2b$_1$ and b$_2$, ESI†).[16,17] The peaks at 284 and 408 cm^{-1} correspond to the bending vibrations of V=O. The peaks at 522 cm^{-1} and 695 cm^{-1} correspond to the stretching vibrations of V$_3$–O and V$_2$–O. Furthermore, the peak at 993 cm^{-1} is attributed to the terminal V=O bond. The XPS spectra of VO$_2$ reveal a minor presence of V^{5+} (Fig. S2c$_1$ and c$_2$, ESI†).

This work performed *in situ* self-transformation in a cell for better repeatability (Fig. 1a and b). The schematic illustration of battery disassembly and the photo of VOH-1 are provided to

Key Laboratory of Physics and Technology for Advanced Batteries, College of Physics, Jilin University, Changchun 130012, P. R. China.
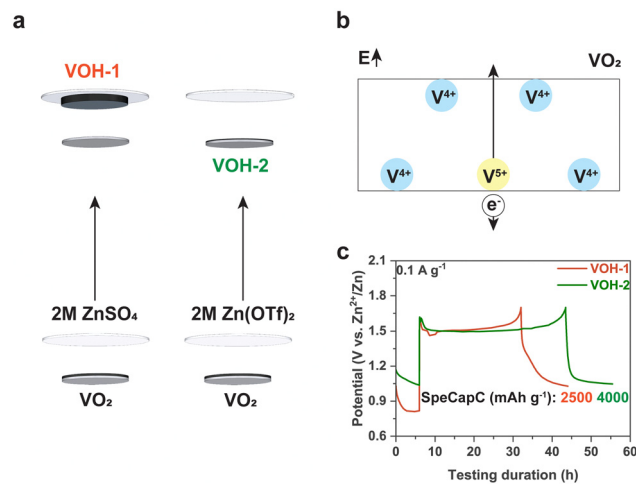*E-mail: shenghan@jlu.edu.cn*

Fig. 1   *In situ* self-transformation. (a) The schematic diagram. (b) The schematic diagram of VOH-1. (c) The time–potential curves.

Fig. 2   The morphological and compositional characterization. (a_1) and (a_2) The SEM images of VOH-1 and the reverse side. (b_1) and (b_2) The SEM images of VOH-2. (c), (a_3) and (b_3) The SEM-EDS elemental maps of the cross section of VO_2, VOH-1 and VOH-2.

facilitate a better understanding of *in situ* self-transformation (Fig. S3a and b, ESI†). Each cell included 80 μl electrolyte and stood for 6 h to reach a steady state before *in situ* self-transformation. A current density of 0.1 A g^{-1} was used to complete *in situ* self-transformation. After a simple test, we opted for a cut-off voltage of 1.7 V and a direct charging scheme (Fig. S3c and d, ESI†). After *in situ* self-transformation, we observed the detachment of VOH-1 from the current collector. The detachment is due to the poor adhesion of PVDF in 2 M $ZnSO_4$ and was also observed in the cells standing for 24 h (Fig. S4, ESI†).

The time-potential curves of *in situ* self-transformation show that both VOH-1 and VOH-2 exhibited prolonged voltage plateaus (Fig. 1c). The number of electrons used to complete *in situ* self-transformation is much greater than that needed for the transition from V^{4+} to V^{5+} (about 300 mA h g^{-1}).[18] This implies that *in situ* self-transformation exhibits significant side reactions, which involve a gas generation process.[19,20] We measured the thickness of cells before and after *in situ* self-transformation, recording 2.45–2.48 mm and 2.55–2.68 mm. The thickness of the cells expanded. This provides additional evidence that the side reactions involve a gas evolution process. The gas evolution process could lead to the formation of a porous structure. However, this process also occurred in VOH-2, where a porous surface structure did not form (Fig. 2a_1 and b_1). This reveals that 2 M $ZnSO_4$ is responsible for the formation of a favorable surface morphology.

We observed that VOH-1 has a close connection with GF and an exposed carbon framework on the reverse side (Fig. 2a_2). To explain this phenomenon, we collected EDS elemental maps in the cross section (Fig. 2c, a_3 and b_3). Compared to the VO_2 electrode, VOH-1 has expanded volume, while VOH-2 shows a reduction in volume. The formation of the divided morphology in VOH-2 is also because of that (Fig. 2b_2). In the VO_2 electrode, V and C were spread evenly. In VOH-1, the carbon framework is retained in the original position, while the V element is distributed within the expanded volume. This implies that *in situ* self-information in 2 M $ZnSO_4$ has a tendency to grow along the electric field.
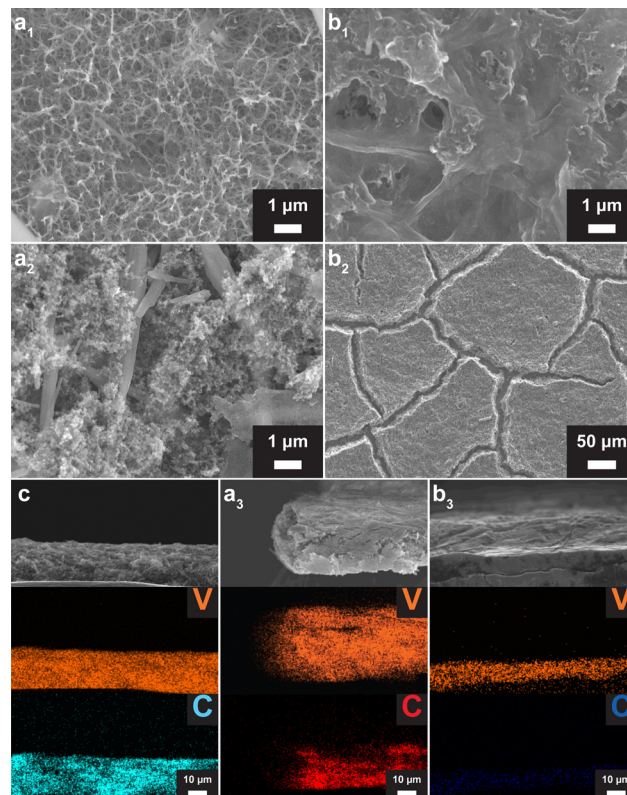
The XRD patterns of VOH-1 and VOH-2 are consistent with previous reports and can be indexed to $V_2O_5 \cdot nH_2O$ (PDF#00-007-0332) (Fig. 3a_1 and b_1).[7,21,22] The TEM images of VOH-1 reveal 0.34 nm lattice fringes, corresponding to the (5 0 0) plane (Fig. S5, ESI†). The XRD peak of the (0 0 1) plane of VOH-1 is almost gone. This implies that the electrolyte environment alters the crystal growth orientation. The Raman spectra of
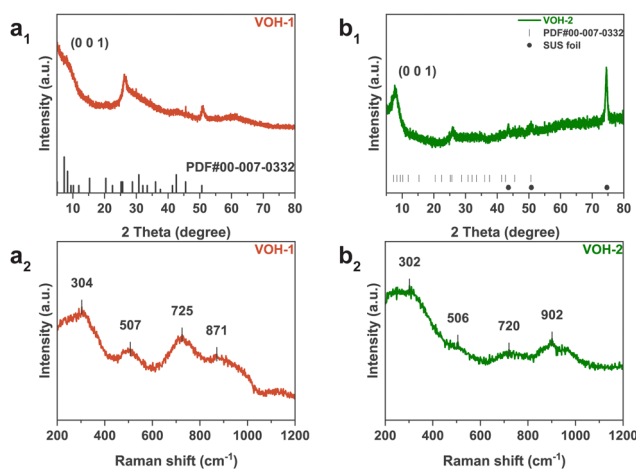

Fig. 3   The structural characterization of VOH-1 and VOH-2. (a_1) and (b_1) XRD patterns. (a_2) and (b_2) Raman spectra.
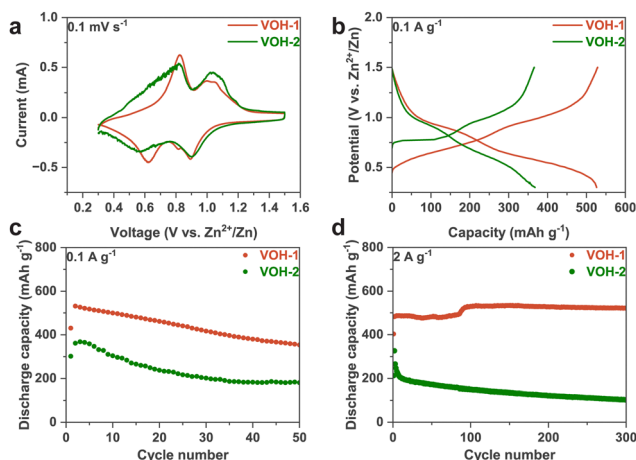
Fig. 4 The electrochemical characterization of VOH-1 and VOH-2. (a) The CV curves of the first cycles. (b) The capacity–potential curves of the second cycles. (c) and (d) The cycling performance.

VOH-1 and VOH-2 are consistent with previous reports (Fig. 3a$_2$ and b$_2$).[2,20,21] The peak at 304 cm^{-1} corresponds to the bending vibration of V=O. The peaks at 507 and 725 cm^{-1} correspond to the stretching vibrations of V$_3$–O and V$_2$–O. These three vibrations are related to the V–O main framework and have nearly the same position. This suggests that VOH-1 and VOH-2 have the same basic structure. The peak at 871 cm^{-1} corresponds to the stretching vibration of V–OH$_2$. This shows that lattice water has been successfully put into the crystal lattice. The XPS spectra of VOH-1 and VOH-2 suggest the presence of V^{4+} (Fig. S6, ESI†).

We proceeded to assemble batteries using VOH-1 and VOH-2, subjecting them to the following electrochemical tests with a voltage window from 0.3 to 1.5 V. The 2 M Zn(OTf)$_2$ electrolyte was chosen, because it is commonly used in vanadium-based batteries. The electrolyte amount of 2 M Zn(OTf)$_2$ was about 90 µl (Fig. S7, ESI†). The CV curves show two primary electrochemical platforms, which are consistent with the capacity-potential curves (Fig. 4a and b). VOH-2 has a pronounced voltage polarization between the oxidation peak and the reduction peak. This suggests that VOH-2 exhibits a worse electrochemical capability. The cycling performance shows the same results (Fig. 4c and d). At a rate of 0.1 A g^{-1}, both VOH-1 and VOH-2 exhibit a significant capacity decay. This phenomenon is quite common in vanadium-based batteries, which is believed to be due to the formation of the electrochemically inactive zinc pyrovanadate phase.[22] VOH-1 exhibits excellent cycling performance. This is attributed to the shorter migration path for Zn^{2+} caused by the porous surface structure and the lower crystallinity along the (0 0 1) plane. At a rate of 2 A g^{-1}, VOH-1 can maintain stable cycling with a capacity of 500 mA h g^{-1} for 1800 cycles (Fig. S8a$_2$, ESI†). Additional electrochemical characterization is presented in Fig. S8 (ESI†).

This work demonstrates the importance of electrolyte environment during *in situ* self-transformation for synthesizing V$_2$O$_5$·nH$_2$O. 2 M ZnSO$_4$ leads to a tendency to grow along the electric field and alters the crystal growth orientation. This causes expanded volume, porous surface morphology and low crystallinity along the (0 0 1) plane and results in excellent cycling performance. 2 M Zn(OTf)$_2$ leads to a volume reduction, making the electrolyte difficult to infiltrate. The importance has been proved by contrasting the production of different electrolytes. This work expands the possibility for *in situ* self-transformation.

Conflicts of interest

There are no conflicts to declare.

Notes and references

1 S. Liu, L. Kang, J. M. Kim, Y. T. Chun, J. Zhang and S. C. Jun, *Adv. Energy Mater.*, 2020, **10**, 2000477.
2 F. Ming, H. Liang, Y. Lei, S. Kandambeth, M. Eddaoudi and H. N. Alshareef, *ACS Energy Lett.*, 2018, **3**, 2602–2609.
3 J. Zhou, L. Shan, Z. Wu, X. Guo, G. Fang and S. Liang, *Chem. Commun.*, 2018, **54**, 4457–4460.
4 S. Deng, Z. Yuan, Z. Tie, C. Wang, L. Song and Z. Niu, *Angew. Chem., Int. Ed.*, 2020, **59**, 22002–22006.
5 H. Jiang, W. Gong, Y. Zhang, X. Liu, M. Waqar, J. Sun, Y. Liu, X. Dong, C. Meng, Z. Pan and J. Wang, *J. Energy Chem.*, 2022, **70**, 52–58.
6 S. Liu, H. Zhu, B. Zhang, G. Li, H. Zhu, Y. Ren, H. Geng, Y. Yang, Q. Liu and C. C. Li, *Adv. Mater.*, 2020, **32**, 2001113.
7 M. Yan, P. He, Y. Chen, S. Wang, Q. Wei, K. Zhao, X. Xu, Q. An, Y. Shuang, Y. Shao, K. T. Mueller, L. Mai, J. Liu and J. Yang, *Adv. Mater.*, 2018, **30**, 1703725.
8 J. Shin, D. S. Choi, H. J. Lee, Y. Jung and J. W. Choi, *Adv. Energy Mater.*, 2019, **9**, 1900083.
9 M. Tian, C. Liu, J. Zheng, X. Jia, E. P. Jahrman, G. T. Seidler, D. Long, M. Atif, M. Alsalhi and G. Cao, *Energy Storage Mater.*, 2020, **29**, 9–16.
10 C. Xia, J. Guo, P. Li, X. Zhang and H. N. Alshareef, *Angew. Chem., Int. Ed.*, 2018, **57**, 3943–3948.
11 Y. Zhang, T. Cheng, Y. Wang, W. Lai, H. Pang and W. Huang, *Adv. Mater.*, 2016, **28**, 5242–5248.
12 G. Yilmaz, K. M. Yam, C. Zhang, H. J. Fan and G. W. Ho, *Adv. Mater.*, 2017, **29**, 1606814.
13 D. Ma, Y. Li, H. Mi, S. Luo, P. Zhang, Z. Lin, J. Li and H. Zhang, *Angew. Chem.*, 2018, **130**, 9039–9043.
14 D. Ma, Y. Li, J. Yang, H. Mi, S. Luo, L. Deng, C. Yan, M. Rauf, P. Zhang, X. Sun, X. Ren, J. Li and H. Zhang, *Adv. Funct. Mater.*, 2018, **28**, 1705537.
15 Y. Zhang, M. Fan, X. Liu, G. Xie, H. Li and C. Huang, *Solid State Commun.*, 2012, **152**, 253–256.
16 J. Chen, B. Xiao, C. Hu, H. Chen, J. Huang, D. Yan and S. Peng, *ACS Appl. Mater. Interfaces*, 2022, **14**, 28760–28768.
17 J. Wang, X. Zhang, Y. Zhang, A. Abas, X. Zhao, Z. Yang, Q. Su, W. Lan and E. Xie, *RSC Adv.*, 2017, **7**, 35558–35564.
18 J.-S. Park, J. H. Jo, Y. Aniskevich, A. Bakavets, G. Ragoisha, E. Streltsov, J. Kim and S.-T. Myung, *Chem. Mater.*, 2018, **30**, 6777–6787.
19 L. Wang, K.-W. Huang, J. Chen and J. Zheng, *Sci. Adv.*, 2019, **5**, eaax4279.
20 H. Luo, B. Wang, F. Wu, J. Jian, K. Yang, F. Jin, B. Cong, Y. Ning, Y. Zhou, D. Wang, H. Liu and S. Dou, *Nano Energy*, 2021, **81**, 105601.
21 Q. Zong, Q. Zhuang, C. Liu, Q. Kang, Y. Wu, J. Zhang, J. Wang, D. Tao, Q. Zhang and G. Cao, *Adv. Energy Mater.*, 2023, **13**, 2301480.
22 Y. Kim, Y. Park, M. Kim, J. Lee, K. J. Kim and J. W. Choi, *Nat. Commun.*, 2022, **13**, 2371.